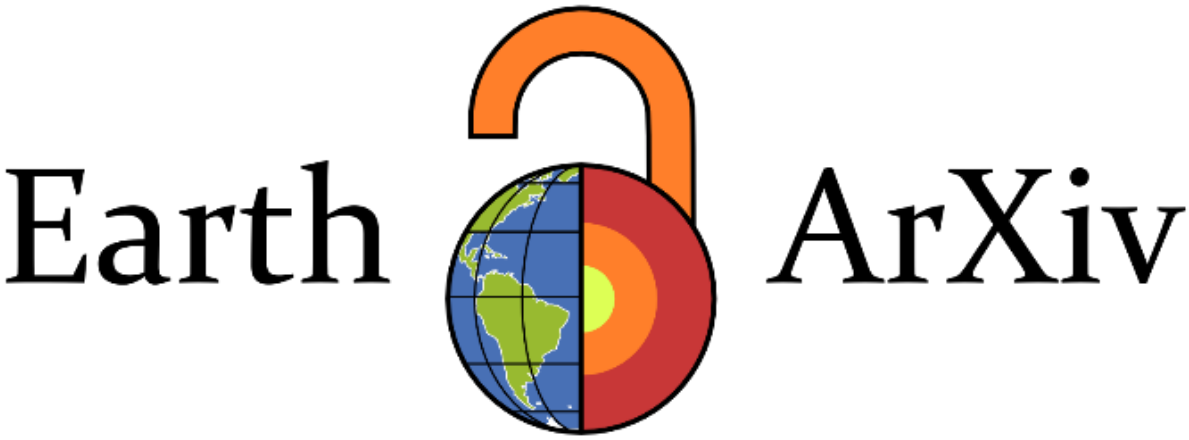

Data-Driven Extraction of Spatiotemporal Causal Networks of Extreme Snowfall Based on Long-Term Observations in the Japanese Archipelago

Hiroshi MATSUDA[1*] and Shin'ichi HOMMA[1]
[1] Kokusai Kogyou Co., Ltd.,

2-24-1, Harumi-cho, Fuchu-shi, Tokyo 183-0057
[*]Corresponding author: hiroshi_matsuda@kk-grp.jp

Abstract

Understanding the spatiotemporal dynamics and long-term trends of extreme weather events is crucial for climate risk assessment. However, extracting causal network structures and underlying trends from observational data remains challenging due to large-scale common influences, spurious correlations, and historical missing values.

In this study, we propose a generalized data-driven framework for extracting spatiotemporal causal network structures and underlying trends by systematically integrating statistical and machine learning techniques. The framework consists of two main stages. First, it employs Graphical Lasso and Markov blanket extraction to reduce the influence of large-scale common factors, followed by the identification of causal structures using a Linear Non-Gaussian Acyclic Model (LiNGAM). Second, it applies robust regression and state-space modeling (Kalman filtering) to mitigate the effects of extreme anomalies and missing values, enabling the extraction of smooth non-linear trends.

As a representative case study, the framework is applied to over a century of annual maximum snow depth records (135 years) in the Japanese archipelago. The results reveal distinct network structures and provide a visualization of meso-scale causal propagation patterns associated with the Japan-Sea Polar-airmass Convergence Zone (JPCZ), as well as localized seesaw relationships influenced by topography. Furthermore, the state-space model identifies a decadal regime shift in the late 1980s, indicating a non-linear decline in extreme snowfall associated with temperature thresholds between snow and rain. These findings demonstrate the applicability of the proposed framework for analyzing complex spatiotemporal dynamics of extreme weather.

Keywords: Extreme snowfall; Japan-Sea Polar-airmass Convergence Zone (JPCZ); climate regime shift; localized seesaw relationships; spatiotemporal causal networks; causal discovery; LiNGAM; Graphical Lasso; state-space model; Kalman filtering; robust regression

1 Introduction

The Japan Sea side of the Japanese archipelago is one of the heaviest snowfall regions in the world. Extreme snowfall in this region is primarily driven by interactions between the cold East Asian winter monsoon originating from the Siberian High and the warm Tsushima Current. These air–sea interactions, combined with forced orographic lifting by the central mountain ranges, lead to the formation and organization of meso-scale snow cloud systems, including the Japan-Sea Polar-airmass Convergence Zone (JPCZ) [15, 18]. As a result, highly localized extreme snowfall events frequently occur.

Given the significant societal and climatological impacts of such events, numerous studies have investigated long-term variations in snowfall and snow depth. Observational analyses [5, 12, 13, 14, 16] have reported decreasing trends in annual maximum snow depth, particularly in relatively warm regions where temperatures are near the threshold between snowfall and rainfall. In addition, numerical simulations and climate projections [6] suggest that extreme daily snowfall may locally increase despite an overall decline in seasonal snowfall under global warming. However, many conventional studies have primarily relied on linear regression or average-based metrics, which are limited in their ability to capture non-linear decadal variability and are sensitive to extreme events and observational noise.

In addition to long-term trends, interannual variability in snowfall exhibits strong regional heterogeneity. This variability is influenced by large-scale atmospheric circulation patterns, such as the East Asian Winter Monsoon Index (MOI), the Arctic Oscillation (AO), and the El Niño–Southern Oscillation (ENSO), as well as teleconnection patterns including the Eurasian (EU) and Western Pacific (WP) structures. Variations in jet streams, atmospheric blocking, and large-scale flow regimes can significantly alter the spatial distribution of snowfall [17]. As a consequence, localized seesaw patterns often emerge, where increased snowfall in one region coincides with reduced snowfall in another. Conventional correlation-based analyses, however, often fail to distinguish such localized relationships from spurious correlations induced by large-scale common drivers, making it difficult to isolate the underlying dependency structures.

To address these challenges, this study proposes a generalized data-driven framework for analyzing spatiotemporal dependency structures and long-term trends in observational data. In the first stage, Graphical Lasso [2] and Markov blanket extraction [7] are employed to reduce the influence of large-scale common factors and identify localized dependency structures. Subsequently, a Linear Non-Gaussian Acyclic Model (LiNGAM) [9, 10] is applied to extract potential causal propagation processes in a data-driven manner. In the second stage, a robust state-space model incorporating robust regression [3] and Kalman filtering [4, 8] is used to mitigate the influence of extreme anomalies and missing values, enabling stable estimation of underlying non-linear trends.

This integrated framework provides a systematic approach for exploring spatiotemporal dependency patterns and their relationship with physical mechanisms underlying extreme snowfall, offering a useful perspective for analyzing complex climate-related phenomena.

Figure 1 illustrates the overall workflow of the proposed framework, which integrates spatial causal network extraction and temporal non-linear trend analysis within a unified pipeline.

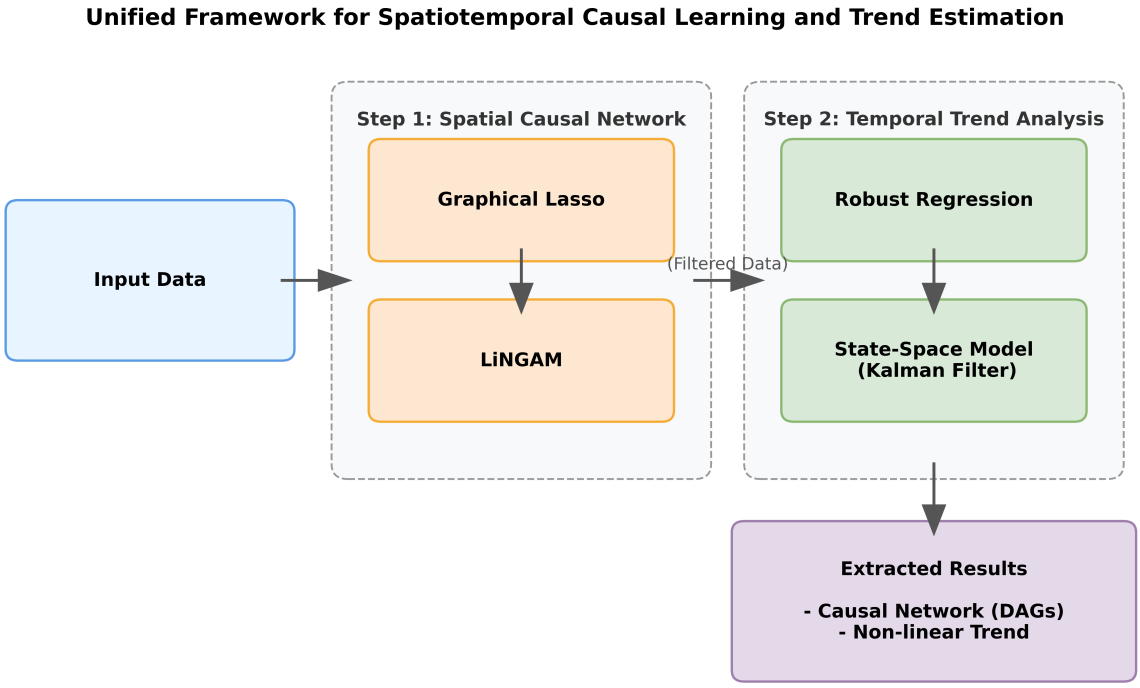

Figure 1: Overview of the proposed unified spatiotemporal machine learning framework. The framework integrates correlation filtering (Graphical Lasso), causal discovery (LiNGAM), and non-linear trend extraction using state-space models within a unified pipeline.

2 Representative Case Study

2.1 Meteorological Background of the Sea of Japan Coast

The coastal region of the Sea of Japan is uniquely characterized by its heavy snowfall, driven by the complex interactions between continental cold air masses and the relatively warm ocean surface. During the boreal winter, the East Asian winter monsoon brings frigid, dry air from the Siberian High. As this cold air flows over the Tsushima Warm Current in the Sea of Japan, it undergoes intense air-sea interactions, acquiring substantial heat and moisture. This process destabilizes the lower troposphere, forming organized meso-scale convective clouds.

A particularly prominent feature in this region is the Japan-Sea Polar-airmass Convergence Zone (JPCZ) [15, 18], a distinct convergence band of snow clouds extending from the base of the Korean Peninsula to the Hokuriku and Niigata regions. The JPCZ frequently causes continuous, localized extreme snowfall. Furthermore, the steep central mountain ranges along the Japanese archipelago force these moist air masses upward, triggering strong orographic precipitation. Variations in large-scale atmospheric circulations passively modulate the landfall locations of these snow bands, often resulting in localized seesaw relationships in snowfall amounts across different regions.

2.2 Observational Dataset

To capture these complex spatiotemporal dynamics and long-term climate regime shifts, this study analyzes a 135-year continuous record (1889–2024) of the annual maximum snow depth. The dataset was obtained from 23 meteorological observation stations distributed widely across the Sea of Japan side, ranging from Hokkaido in the north to the San-in region in the south (Figure 2).

Annual maximum snow depth is a critical indicator for evaluating the intensity of extreme historical snowfall events and their socioeconomic impacts. However, such long-term historical records inherently contain substantial non-Gaussian fluctuations, extreme outliers due to rare heavy snow years, and missing values. Therefore, applying conventional linear analysis to this dataset is insufficient; it necessitates advanced robust data-driven modeling to reveal the true underlying climate states and pure causal propagation networks.

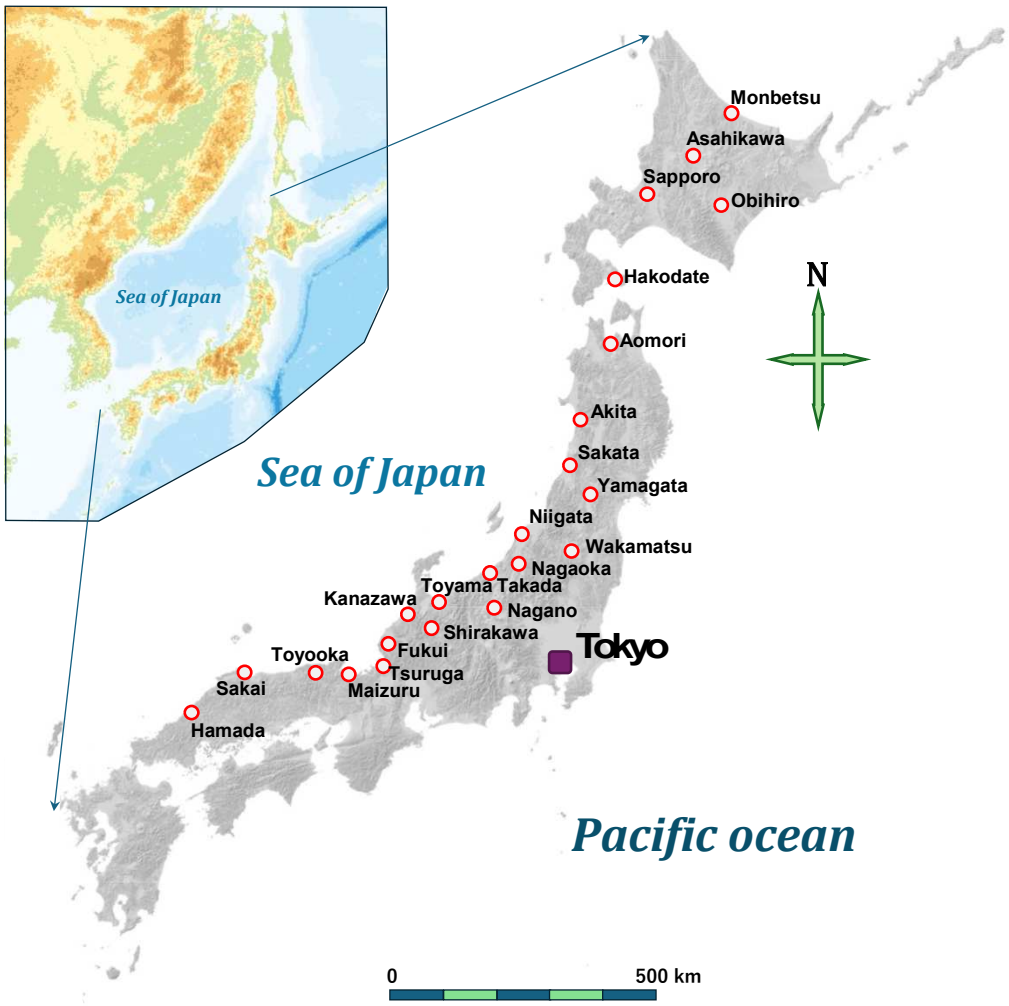

Figure 2: Locations of the 23 observation stations in the Japan-Sea side area. Red circles indicate the locations of the 23 observation stations. The topographic map is based on the electronic maps of the Geospatial Information Authority of Japan.

Table 1 summarizes the detailed geographical information, observation periods, and the number of missing years for the 23 selected stations.

Table 1: Description of the 23 observation stations in the Sea of Japan side of Japan.

Abbr.	Station Name	Latitude	Longitude	Elevation (m)	Period	Missing (yrs)
Mb	Mombetsu	44°20′N	143°21′E	15.8	1904–2024	9
As	Asahikawa	43°45′N	142°22′E	119.8	1893–2024	0
Sp	Sapporo	43°03′N	141°19′E	17.4	1889–2024	0
Ob	Obihiro	42°55′N	143°12′E	38.4	1891–2024	0
Hd	Hakodate	41°49′N	140°45′E	35.0	1890–2024	0
Ao	Aomori	40°49′N	140°46′E	2.8	1895–2024	0
Ak	Akita	39°43′N	140°05′E	6.3	1889–2024	0
Sk	Sakata	38°54′N	139°50′E	3.1	1900–2024	5
Ym	Yamagata	38°15′N	140°20′E	152.5	1892–2024	0
Wk	Wakamatsu	37°29′N	139°54′E	211.7	1911–2024	1
Ni	Niigata	37°54′N	139°02′E	1.9	1890–2024	4
Ng	Nagaoka	37°45′N	138°50′E	23.0	1889–2024	1
Tk	Takada	37°06′N	138°14′E	12.9	1921–2024	0
Nn	Nagano	36°39′N	138°11′E	418.2	1891–2024	0
Ty	Toyama	36°42′N	137°12′E	8.6	1938–2024	0
Sr	Shirakawa	36°27′N	136°53′E	478.0	1915–2024	0
Kz	Kanazawa	36°35′N	136°38′E	5.7	1890–2024	0
Fk	Fukui	36°03′N	136°13′E	8.8	1897–2024	0
Ts	Tsuruga	35°39′N	136°03′E	1.6	1897–2024	0
Mz	Maizuru	35°27′N	135°19′E	2.4	1912–2024	3
To	Toyooka	35°32′N	134°49′E	3.4	1917–2024	1
Sa	Sakai	35°32′N	133°14′E	2.0	1893–2024	0
Hm	Hamada	34°53′N	132°04′E	19.0	1892–2024	0

2.3 Long-term Trends and Limitations of Linear Analysis

To highlight the limitations of conventional analytical approaches, Figure **??** presents the long-term trends of the annual maximum snow depth estimated using ordinary least squares (OLS) regression for all 23 stations. As is evident from the figure, the simple linear regression lines (red dashed lines) are strongly influenced by extreme historical outliers, such as the unprecedented heavy snowfalls in 1963 and 1981, as well as missing values. Consequently, these conventional linear estimates make it difficult to accurately recover the true underlying trend structure and decadal climate regime shifts hidden in the data. This fundamental limitation underscores the crucial necessity of applying advanced, robust data-driven modeling—which will be introduced in Section 3—to extract the pure climate states.

Figure 3 presents long-term trends estimated using ordinary least squares (OLS). These estimates are significantly affected by extreme outliers and missing values, making it difficult to recover the underlying trend structure. This highlights the limitations of conventional approaches when applied to noisy spatiotemporal data spanning long time periods.

Table A1 shows that strong correlations are widely observed across stations, reflecting the influence of macroscopic common factors. In contrast, Table A2 illustrates localized dependency structures after filtering these spurious correlations, providing the basis for subsequent causal network analysis.

These results illustrate the limitations of conventional approaches and motivate the need for a more sophisticated data-driven framework capable of extracting underlying causal structures and non-linear trends.

These results provide the foundation for applying the proposed causal discovery and trend extraction framework described in the following section.

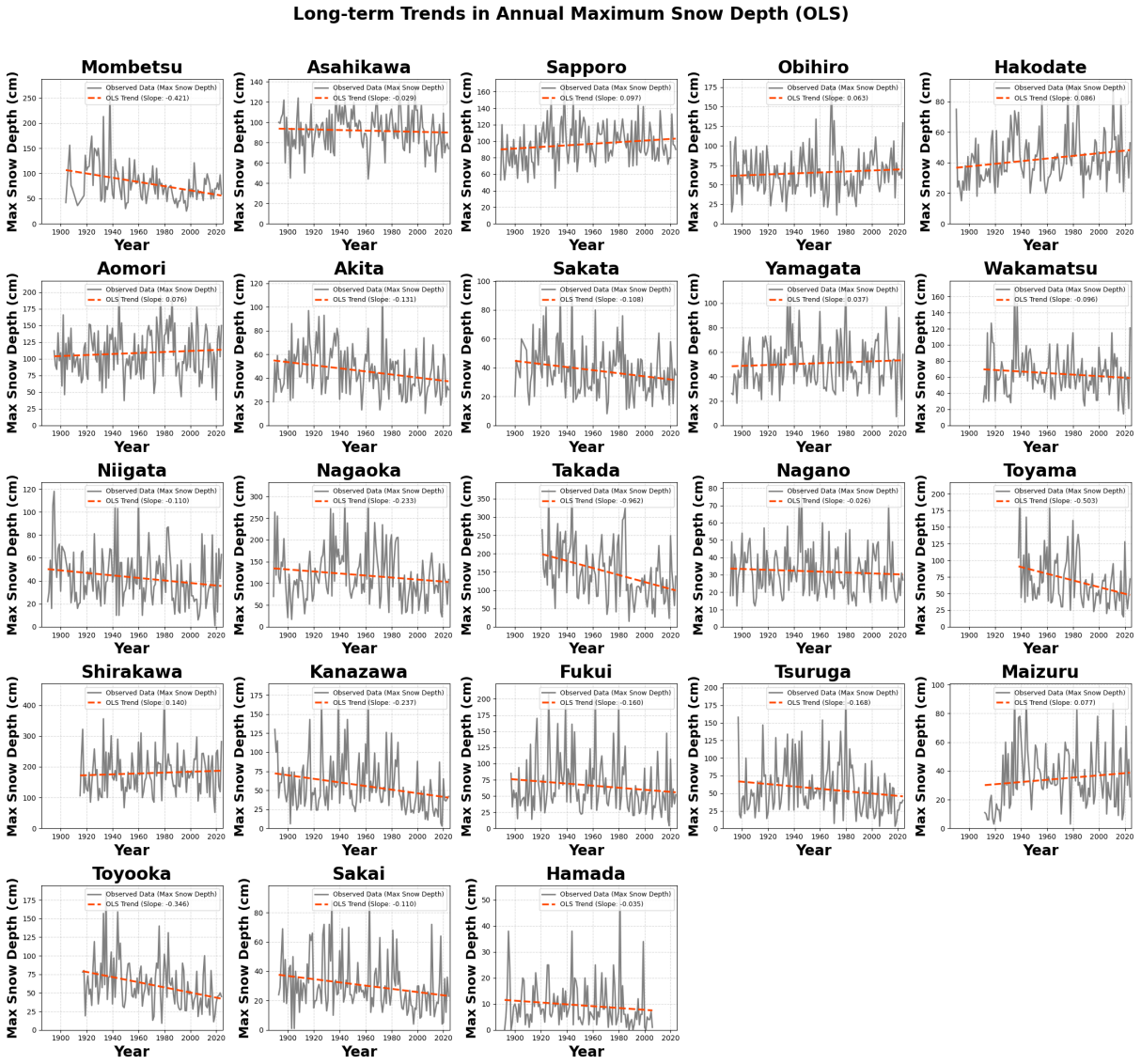

Figure 3: Long-term trends in annual maximum snow depth using ordinary least squares (OLS) regression for the 23 stations. Gray solid lines represent the observed annual maximum snow depth, while red dashed lines indicate the estimated linear trends.

3 Methodology

Unlike conventional approaches that treat correlation filtering, causal discovery, and trend estimation as separate tasks, the proposed framework unifies these components into a single coherent pipeline. This integration enables consistent extraction of spatiotemporal causal structures and underlying trends while systematically mitigating the effects of confounding factors, noise, and missing data.

This section describes the mathematical formulation and detailed computational processes of the integrated framework proposed in this study for spatiotemporal data analysis.

3.1 Causal Candidate Extraction via Graphical Lasso

In multivariate data, the partial correlation coefficient $\rho_{jk \cdot others}$ between variables X_j and X_k is used as a measure of conditional independence given all other variables. Let $\Theta = \Sigma^{-1}$ be the inverse of the covariance matrix (precision matrix) with its elements denoted by θ_{jk}. The partial correlation coefficient is expressed as:

$$\rho_{jk \cdot others} = -\frac{\theta_{jk}}{\sqrt{\theta_{jj}\theta_{kk}}} \tag{1}$$

To enforce sparsity and shrink weak, potentially spurious correlations toward zero, we apply the Graphical Lasso [2] with L1 regularization to extract a meaningful sparse network. Under the assumption that n independent observations follow a multivariate normal distribution, and letting S be the empirical covariance matrix, the log-likelihood function $\ell(\Theta)$ of the precision matrix Θ is given by:

$$\ell(\Theta) = \frac{n}{2}\log\det(\Theta) - \frac{1}{2}\sum_{i=1}^{n}(x_i - \bar{x})^T\Theta(x_i - \bar{x}) - \frac{np}{2}\log(2\pi) \tag{2}$$

By utilizing the cyclic property of the trace operator ($\mathrm{tr}(ABC) = \mathrm{tr}(CAB)$), the second term of Equation 2 can be analytically rewritten using the empirical covariance matrix S:

$$\frac{1}{n}\sum_{i=1}^{n}(x_i - \bar{x})^T\Theta(x_i - \bar{x}) = \mathrm{tr}(S\Theta) \tag{3}$$

Therefore, maximizing the log-likelihood is equivalent to minimizing the negative log-likelihood $L(\Theta) = \mathrm{tr}(S\Theta) - \log\det(\Theta)$. To enforce sparsity, the Graphical Lasso optimizes the objective function with an L1 penalty on the off-diagonal elements:

$$\hat{\Theta} = \arg\min_{\Theta \succ 0}\left(\mathrm{tr}(S\Theta) - \log\det(\Theta) + \lambda\sum_{j \neq k}|\theta_{jk}|\right) \tag{4}$$

where λ is a tuning parameter controlling the penalty strength, and $\Theta \succ 0$ ensures the positive definiteness of the precision matrix.

From the extracted precision matrix $\hat{\Theta}$, we identify the Markov Blanket (MB) [7], which is the minimal set of variables having a direct dependency structure with a specific target variable X_j. It is strictly extracted as the set of non-zero elements in the corresponding row of $\hat{\Theta}$:

$$MB(X_j) = \{X_k \mid \hat{\theta}_{jk} \neq 0 \ (k \neq j)\} \tag{5}$$

3.2 Identification of Causal Propagation Processes via LiNGAM

After eliminating macroscopic spurious correlations using the Markov blanket, we apply the Linear Non-Gaussian Acyclic Model (LiNGAM) [9, 10] to determine the causal directionality in a data-driven manner. Let x be the observed variable vector and e be the exogenous variable vector (external influences). The basic LiNGAM model is expressed as:

$$x = Bx + e \tag{6}$$

where B is the adjacency matrix containing the causal connection coefficients. Under the assumption of a directed acyclic graph (DAG), the diagonal elements of B are strictly zero, and if the true causal order is known, B can be permuted into a strictly lower triangular matrix.

Solving Equation 6 for x yields:

$$x = (I - B)^{-1}e = Ae \tag{7}$$

Assuming that the exogenous variables e are mutually independent and follow non-Gaussian distributions, Equation 7 represents the standard Independent Component Analysis (ICA) model, where $A = (I - B)^{-1}$ represents the unknown mixing matrix.

Standard ICA algorithms estimate the separating matrix $W \approx A^{-1} = I - B$. However, ICA has two fundamental indeterminacies: it cannot identify the "permutation" and the "scaling" of the independent components. That is, the output of ICA is given by:

$$W_{ICA} = PDW_{true} = PD(I - B) \tag{8}$$

where P is an unknown permutation matrix and D is an unknown diagonal scaling matrix. LiNGAM resolves these two indeterminacies uniquely by utilizing the structural constraints of the DAG. Since the diagonal elements of the true connection matrix B are zero, the diagonal elements of the true separating matrix $W_{true} = I - B$ must be strictly equal to 1.

First, to resolve the permutation indeterminacy, we seek a permutation matrix $\tilde{P}$ that permutes the rows of W_{ICA} to produce a matrix $\tilde{W}$ containing no zero elements on its main diagonal. This is achieved by minimizing the following cost function:

$$\tilde{W} = \tilde{P}W_{ICA} \quad \text{s.t.} \quad \tilde{P} = \arg\min_{P} \sum_{i} \frac{1}{|(\tilde{P}W_{ICA})_{ii}|} \tag{9}$$

Second, to resolve the scaling indeterminacy, we divide each row of $\tilde{W}$ by its diagonal element to construct a new matrix $\tilde{W}'$ whose diagonal elements are strictly 1:

$$\tilde{W}' = \tilde{D}\tilde{W} \quad \text{where} \quad \tilde{D}_{ii} = \frac{1}{\tilde{W}_{ii}} \tag{10}$$

With both indeterminacies resolved, the true connection coefficient matrix $\hat{B}$ can be recovered as:

$$\hat{B} = I - \tilde{W}' \tag{11}$$

Furthermore, to identify the potential causal propagation process (i.e., the causal order of the variables), we utilize the properties of the DAG. If it is a true DAG, there exists a permutation of variables (a permutation matrix P_{DAG}) such that the connection matrix becomes a strictly lower triangular matrix. We estimate the causal order by finding the optimal permutation matrix $\hat{P}_{DAG}$ that minimizes the sum of absolute values of the upper triangular elements of the permuted matrix:

$$\hat{P}_{DAG} = \arg\min_{P} \sum_{i \leq j} \left| \left(P\hat{B}P^{T} \right)_{ij} \right| \tag{12}$$

By applying this optimal permutation, the final causal connection matrix B_{lower}, representing the cascading propagation process, is obtained as:

$$B_{lower} = \hat{P}_{DAG}\hat{B}\hat{P}_{DAG}^{T} \tag{13}$$

This procedure enables the identification of causal directionality in a fully data-driven manner under non-Gaussian assumptions [9, 10].

3.3 Non-linear Trend Extraction via Robust State-Space Models

To extract the true underlying trend from noisy time-series data, we introduce a two-stage framework that integrates spatial causal analysis and temporal trend estimation using robust regression and state-space modeling.

3.3.1 Robust Regression via Iteratively Reweighted Least Squares (IRLS)

In robust M-estimation [3], which eliminates the influence of extreme outliers such as record-breaking heavy snowfall years, the regression parameter β is estimated to satisfy the following estimating equation:

$$\sum_{i=1}^{n} \psi(Y_i - \beta^T X_i) X_i = 0 \tag{14}$$

where $\psi(x)$ is the derivative of the loss function. To solve this non-linear equation, the Iteratively Reweighted Least Squares (IRLS) method is used. The weight function $W(x)$ is strictly defined as:

$$W(x) = \begin{cases} \psi(x)/x & (x \neq 0) \\ \psi'(0) & (x = 0) \end{cases} \tag{15}$$

In the Huber loss function adopted in this study, the tuning parameter c is set as $c = 1.345\hat{\sigma}$, using a robust estimator $\hat{\sigma}$ of the standard deviation.

Letting X be the design matrix, Y the response vector, and $W^{(m)}$ the diagonal weight matrix at iteration step m, the parameter β is iteratively updated in the form of weighted least squares:

$$\beta^{(m+1)} = (X^T W^{(m)} X)^{-1} X^T W^{(m)} Y \tag{16}$$

3.3.2 State-Space Modeling and Kalman Filtering/Smoothing

To extract smooth, decadal non-linear trends (latent states) and probabilistically interpolate historical missing values, a local level model is introduced. Let y_t be the observed value at time t, and α_t be the true, unobservable climate state. The observation equation and the state equation are defined as:

$$y_t = \alpha_t + \varepsilon_t, \quad \varepsilon_t \sim N(0, \sigma_\varepsilon^2) \tag{17}$$

$$\alpha_{t+1} = \alpha_t + \eta_t, \quad \eta_t \sim N(0, \sigma_\eta^2) \tag{18}$$

A sequential calculation algorithm of the Kalman filter [4, 8] is applied to these equations. The one-step-ahead prediction error (innovation) v_t and its variance F_t are obtained as:

$$v_t = y_t - a_t, \quad F_t = P_t + \sigma_\varepsilon^2 \tag{19}$$

Using these, the Kalman gain $K_t = P_t/F_t$ is calculated, and the filtered state estimate $a_{t|t}$ and the one-step-ahead prediction a_{t+1} are updated:

$$a_{t|t} = a_t + K_t v_t, \quad P_{t|t} = P_t(1 - K_t) \tag{20}$$

$$a_{t+1} = a_{t|t}, \quad P_{t+1} = P_{t|t} + \sigma_\eta^2 \tag{21}$$

Handling Missing Values: A decisive advantage of this state-space model lies in its mathematically rigorous treatment of missing values. When an observation y_t is missing at time t, it is theoretically equivalent to setting the observation variance $\sigma_\varepsilon^2 \to \infty$, resulting in a Kalman gain of exactly zero ($K_t \to 0$). Consequently, Equations 20 and 21 degenerate to:

$$a_{t+1} = a_t, \quad P_{t+1} = P_t + \sigma_\eta^2 \tag{22}$$

This demonstrates the underlying mechanism whereby the state estimate remains constant during missing periods, while the associated uncertainty increases.

Finally, to obtain a more accurate smoothed state $\hat{\alpha}_t$ given all observational data, a backward recurrence of state smoothing is executed. The auxiliary variables r_t and N_t are computed in reverse order (terms involving v_t and F_t^{-1} are treated as zero during missing periods):

$$r_{t-1} = F_t^{-1} v_t + (1 - K_t) r_t \tag{23}$$

$$N_{t-1} = F_t^{-1} + (1 - K_t)^2 N_t \tag{24}$$

Using these, the state smoothed estimate $\hat{\alpha}_t$ and its variance V_t are obtained:

$$\hat{\alpha}_t = a_t + P_t r_{t-1}, \quad V_t = P_t - P_t^2 N_{t-1} \tag{25}$$

This backward smoothing algorithm allows future information to propagate backward into missing periods, seamlessly interpolating the latent climate state while appropriately inflating the variance V_t to reflect uncertainty.

4 Results and Discussion

In this section, we present the application of the proposed framework to the 135-year annual maximum snow depth dataset. Rather than merely demonstrating algorithmic performance, our primary focus is on interpreting the extracted causal structures and non-linear trends from a meteorological and climatological perspective. Specifically, we investigate the spatial extent of the Japan-Sea Polar-airmass Convergence Zone (JPCZ), the meso-scale causal propagation processes of extreme snowfall, and the decadal climate regime shifts hidden beneath severe observational noise.

4.1 Spatial Dependency and Elimination of Macroscopic Confounding Factors

In the context of extreme snowfall along the Sea of Japan, conventional simple correlation analyses often fail to capture the true underlying meteorological dynamics. Because massive macroscopic factors, such as the Siberian cold air mass and the East Asian winter monsoon, simultaneously bring cold temperatures to the entire Japanese archipelago, simple correlation networks generally exhibit strong, spurious synchronization across nearly all observation stations (as shown in the simple correlation matrix, Table A1). Consequently, these macroscopic confounding factors obscure the true, localized causal propagation processes.

To systematically eliminate these macroscopic "base-lifting" effects, we applied the Graphical Lasso to the 135-year dataset. Figure 4 illustrates the extracted partial correlation network, and Figure 5 maps these connections onto the actual geographical coordinates. By mathematically removing the macroscopic common factors, the resulting network effectively isolates the pure, localized synchronizations driven by meso-scale weather systems, such as the Japan-Sea Polar-airmass Convergence Zone (JPCZ) and topographically forced orographic precipitation.

To further investigate the localized dependency structure, Figure 6 presents the Markov blanket extracted specifically for Kanazawa, a representative station in the core heavy snowfall region. The Markov blanket successfully eliminates distant spurious correlations, revealing strong, direct positive synchronizations with adjacent areas heavily influenced by the JPCZ (e.g., Fukui, Shirakawa, Toyama, and Nagaoka). This indicates that these regions are fundamentally governed by the continuous inland propagation of the same snow cloud bands.

The Markov blanket analysis also reveals the existence of a direct negative partial correlation (a "seesaw" relationship) between Kanazawa and geographically distant regions, such as Hokkaido (Sapporo and Hakodate) and the San'in region (Sakai). From a climatological perspective, these localized seesaw relationships are highly consistent with the passive shifting of snowfall zones associated with large-scale atmospheric circulation and teleconnection fluctuations, such as the Eurasian (EU) and Western Pacific (WP) patterns. This demonstrates that our data-driven approach allows for the objective extraction of not only the simple spatial extent of the JPCZ (Sea of Japan Polar Air Mass Convergence Zone) but also the influence of macro-scale atmospheric circulation.

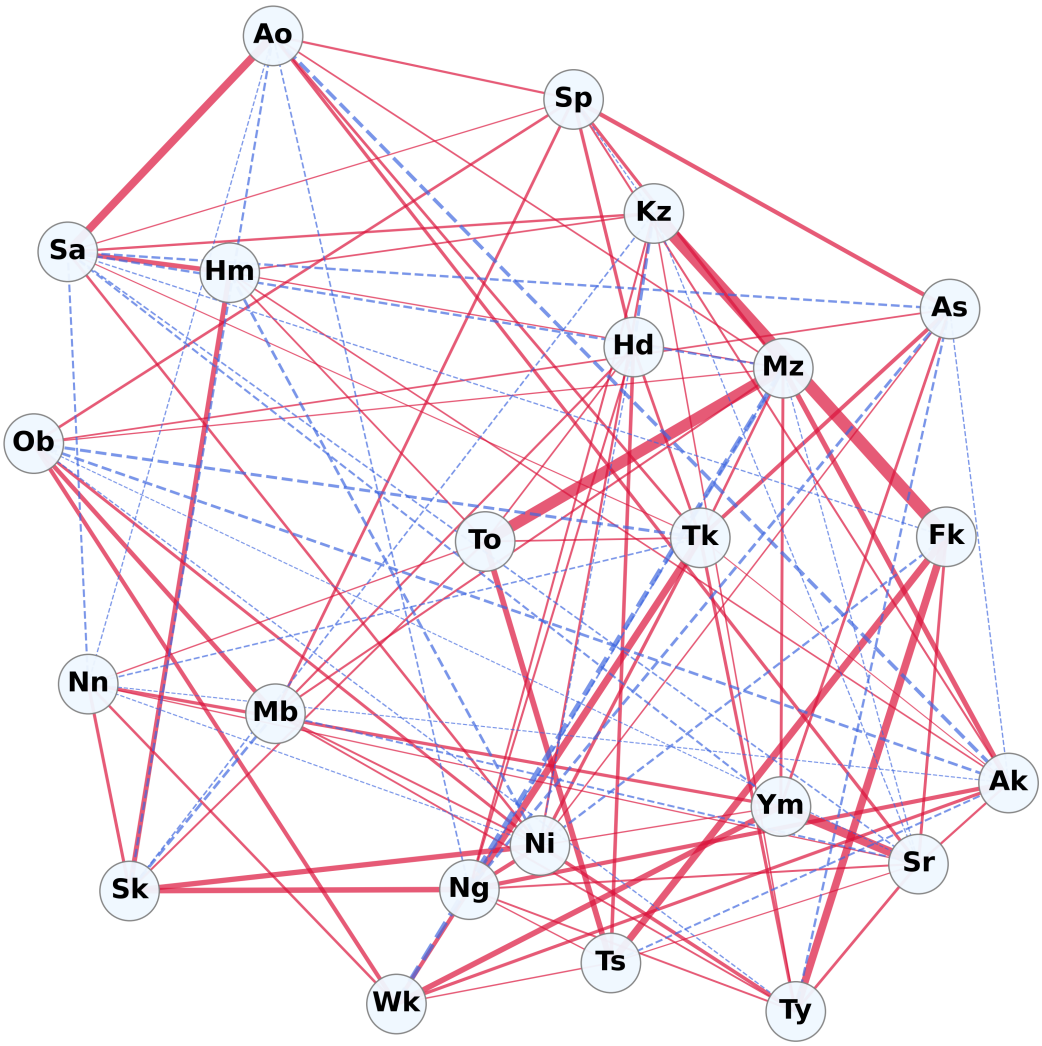

Figure 4: Partial correlation network of the 23 observation stations extracted by the Graphical Lasso. Red solid lines indicate positive partial correlations, while blue dashed lines indicate negative partial correlations. The two-letter abbreviations correspond to the following stations: Mb: Mombetsu, As: Asahikawa, Sp: Sapporo, Ob: Obihiro, Hd: Hakodate, Ao: Aomori, Ak: Akita, Sk: Sakata, Ym: Yamagata, Wk: Wakamatsu, Ni: Niigata, Ng: Nagaoka, Tk: Takada, Nn: Nagano, Ty: Toyama, Sr: Shirakawa, Kz: Kanazawa, Fk: Fukui, Ts: Tsuruga, Mz: Maizuru, To: Toyooka, Sa: Sakai, and Hm: Hamada.

Furthermore, Figure 6 illustrates the Markov blanket extracted targeting "Kanazawa (Kz)", the center of the heavy snowfall region. These results demonstrate that the proposed framework effectively reduces the influence of macroscopic spurious correlations and reveals localized dependency structures.

As shown in Figure 6, the proposed framework reduces the effects of distant dependencies and highlights strong local synchronization patterns (solid red lines) between nearby stations centered in the Hokuriku region such as Fukui, Toyama, and Nagaoka. A local seesaw relationship (negative partial correlation, blue dashed line) was also confirmed between Hokkaido (Sapporo, Hakodate), Tohoku (Sakata), and some mountainous areas in the Chubu region (Shirakawa).

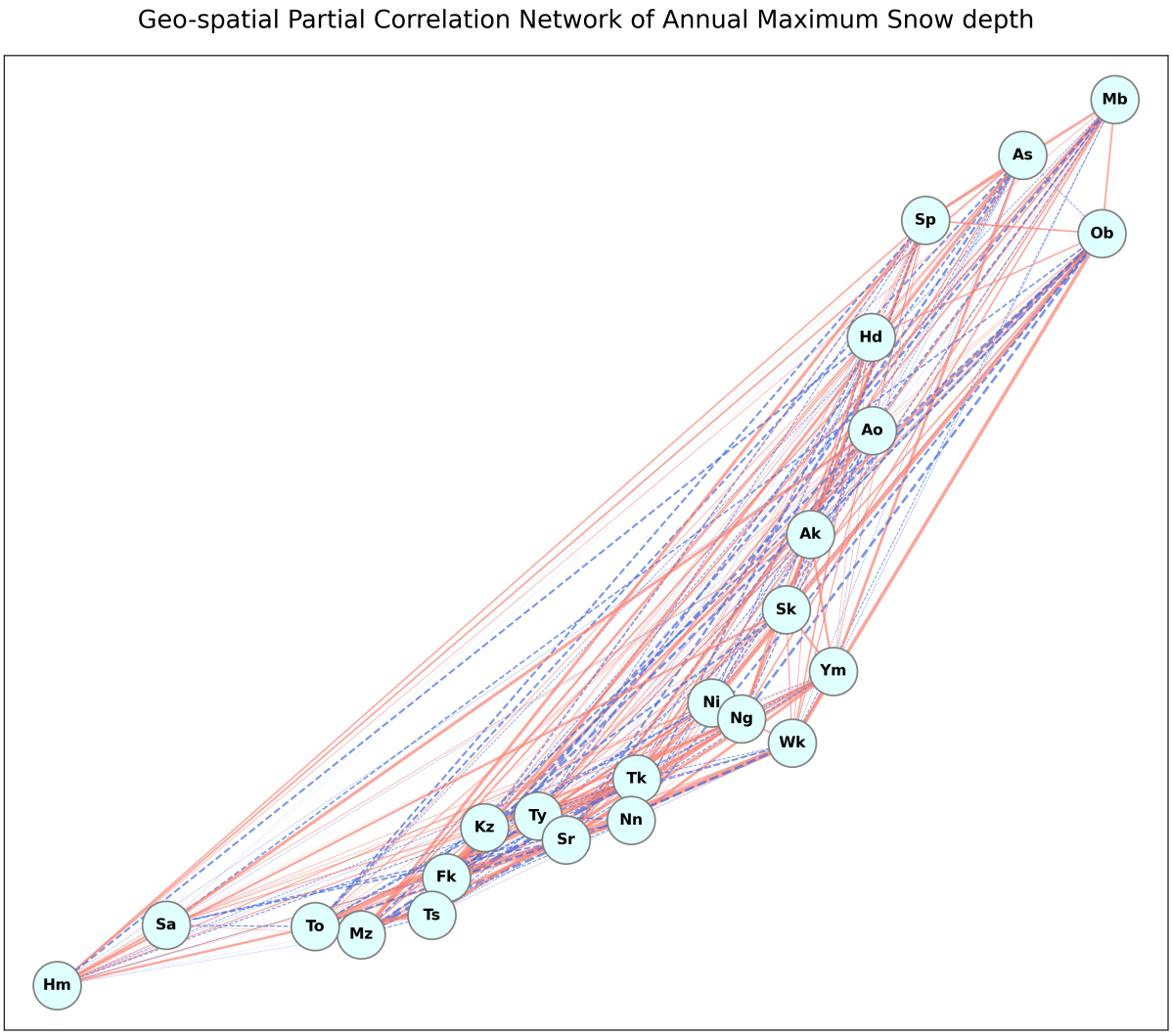

Figure 5: Geo-spatial Partial Correlation Network of Extreme Snowfall. The connections are mapped onto actual geographical coordinates, revealing spatial dependency structures. Red solid lines indicate positive partial correlations, while blue dashed lines indicate negative partial correlations. The two-letter abbreviations correspond to the following stations: Mb: Mombetsu, As: Asahikawa, Sp: Sapporo, Ob: Obihiro, Hd: Hakodate, Ao: Aomori, Ak: Akita, Sk: Sakata, Ym: Yamagata, Wk: Wakamatsu, Ni: Niigata, Ng: Nagaoka, Tk: Takada, Nn: Nagano, Ty: Toyama, Sr: Shirakawa, Kz: Kanazawa, Fk: Fukui, Ts: Tsuruga, Mz: Maizuru, To: Toyooka, Sa: Sakai, and Hm: Hamada.

These results demonstrate that the proposed method effectively captures spatial dependence structures consistent with large-scale fluctuation patterns.

To provide a comprehensive perspective, the Markov blankets extracted individually for all 23 observation stations are presented in Appendix A (Figure A1). Figure A1 confirms that the entire coastal area along the Sea of Japan can be systematically divided into several localized subnetworks based on direct causal candidates, with reduced influence of macroscopic spurious correlations.

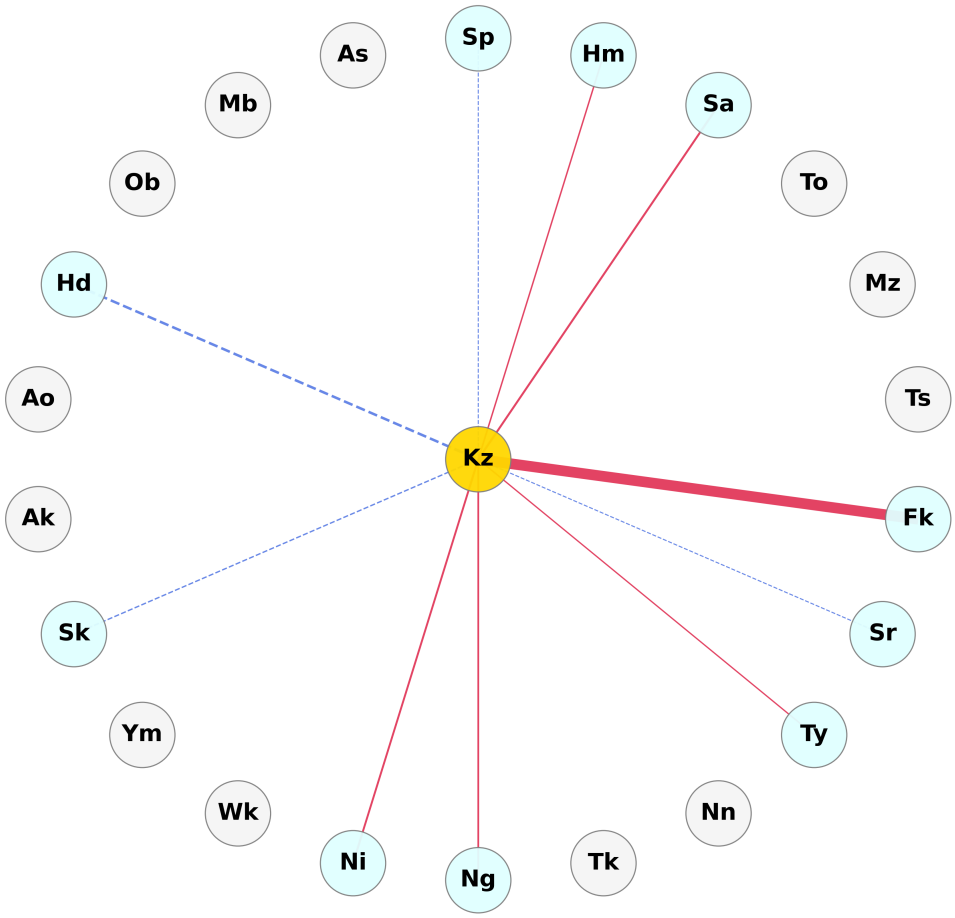

Figure 6: Markov blanket extracted targeting "Kanazawa (Kz)", revealing localized causal candidates with reduced influence of macroscopic spurious correlations.Red solid lines indicate positive partial correlations, while blue dashed lines indicate negative partial correlations. The two-letter abbreviations correspond to the following stations: Mb: Mombetsu, As: Asahikawa, Sp: Sapporo, Ob: Obihiro, Hd: Hakodate, Ao: Aomori, Ak: Akita, Sk: Sakata, Ym: Yamagata, Wk: Wakamatsu, Ni: Niigata, Ng: Nagaoka, Tk: Takada, Nn: Nagano, Ty: Toyama, Sr: Shirakawa, Kz: Kanazawa, Fk: Fukui, Ts: Tsuruga, Mz: Maizuru, To: Toyooka, Sa: Sakai, and Hm: Hamada.

4.2 Meso-scale Causal Propagation and Localized Seesaw Relationships

In the second stage of our framework, we applied LiNGAM to each of the identified subnetworks to determine the causal directionality and quantify the connection strengths. Figures 7, 8, and 9 illustrate the extracted Directed Acyclic Graphs (DAGs) for the Hokkaido, Hokuriku and Niigata, and San-in areas, respectively. The non-Gaussianity of the extreme snowfall data allows us to uniquely identify the cascade of weather systems without relying on arbitrary temporal lagging.

It is important to emphasize that the arrows in these DAGs do not simply represent the physical movement of individual snow clouds within a few hours. Rather, because the input data are annual maximum snow depths, the causal directions mathematically visualize the sequential order of meteorological processes that determine the severity of extreme snowfall for that entire winter. These causal links explicitly capture the continuous inland propagation of weather systems and the complex topographical filter effects (e.g., wind shadows) that dictate the ultimate localized snowfall amounts. We describe the specific dynamics for each of the three isolated subnetworks as follows:

(a) Hokkaido Area (Independent System) Figure 7 illustrates the causal structure in the Hokkaido region. This DAG (Directed Acyclic Graph) provides physical evidence for local seesaw relationships driven by topographical features. Specifically, positive causal relationships (solid red lines) are indicated from Sapporo—on the Sea of Japan side—to Asahikawa, Hakodate, and Obihiro, while negative causal relationships (dashed blue lines) are shown from Mombetsu to Obihiro and from Asahikawa to Obihiro. This indicates that when winter monsoons bring heavy snowfall to windward coastal areas, the amount of snowfall fluctuates locally due to the topographical effects of central mountain ranges, such as the Hidaka and Ishikari Mountains.

(b) Hokuriku and Niigata Area (Core System) Figure 8 illustrates the core system of heavy snowfall along the Japan-Sea coast. The DAG reveals a clear, continuous inland propagation of positive causal connections (red solid lines) originating from coastal stations (e.g., Kanazawa and Niigata) toward inland and mountainous regions (e.g., Takada and Shirakawa). From a meteorological perspective, this quantitative sequence perfectly captures the meso-scale dynamics of the JPCZ: organized transverse snow bands make landfall and are forced upward by the steep central mountain ranges, resulting in simultaneous and amplified orographic precipitation along the windward slopes.

It should be noted that the extracted causal order, such as KANAZAWA $\rightarrow$ TAKADA $\rightarrow$ TOYAMA, may seem counterintuitive from a simple geographical west-to-east perspective. However, this perfectly captures the complex wind shadow effects caused by the topographical features, particularly the Noto Peninsula. The ultimate snowfall amount in Toyama is largely governed by the monsoon wind directions filtered by this peninsula, making it a downstream consequence in the complex causal network rather than a mere geographical neighbor.

(c) San-in Area (Terminal System) Conversely, the San-in area (Figure 9) exhibits a purely positive synchronization network. The absence of negative connections indicates that these terminal regions are uniformly exposed to the same cold air mass outbreaks, resulting in simultaneous snowfall without severe topographical shielding within this specific subnetwork.

These results emphasize that our data-driven approach not only successfully traces the continuous inland propagation of JPCZ snow clouds but also objectively visualizes complex meso-scale thermodynamic processes purely from observational data.

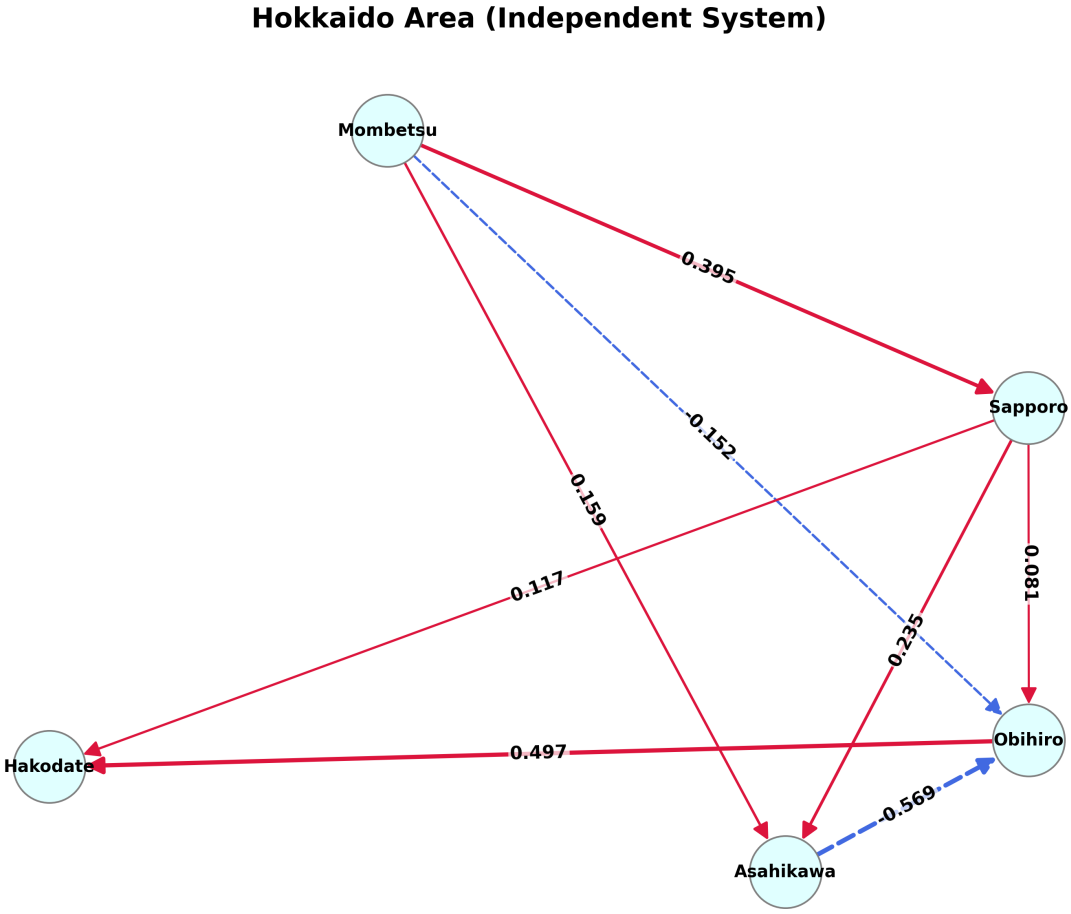

Figure 7: Directed Acyclic Graph (DAG) of the extreme snowfall extracted by LiNGAM for the Hokkaido Area (Independent System), revealing the causal wave propagation processes within this localized sub-network. The thickness of the arrows indicates the magnitude of the connection coefficients. Red solid arrows denote positive connection coefficients, implying strong positive synchronization and simultaneous amplification under the same weather system. Blue dashed arrows indicate negative connection coefficients, representing a localized seesaw relationship.

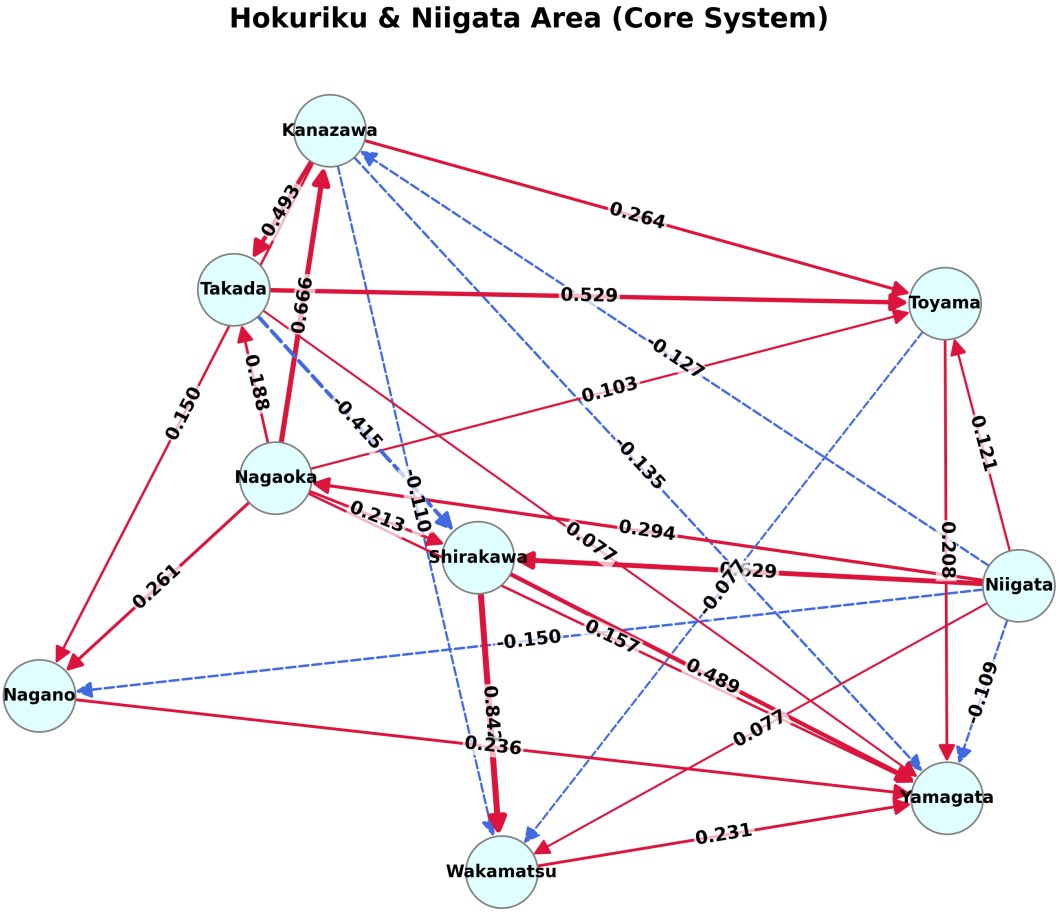

Figure 8: Directed Acyclic Graph (DAG) of the extreme snowfall extracted by LiNGAM for the Hokuriku and Niigata Area (Core System), revealing the causal wave propagation processes within this localized sub-network. The thickness of the arrows indicates the magnitude of the connection coefficients. Red solid arrows denote positive connection coefficients, implying strong positive synchronization and simultaneous amplification under the same weather system. Blue dashed arrows indicate negative connection coefficients, representing a localized seesaw relationship.

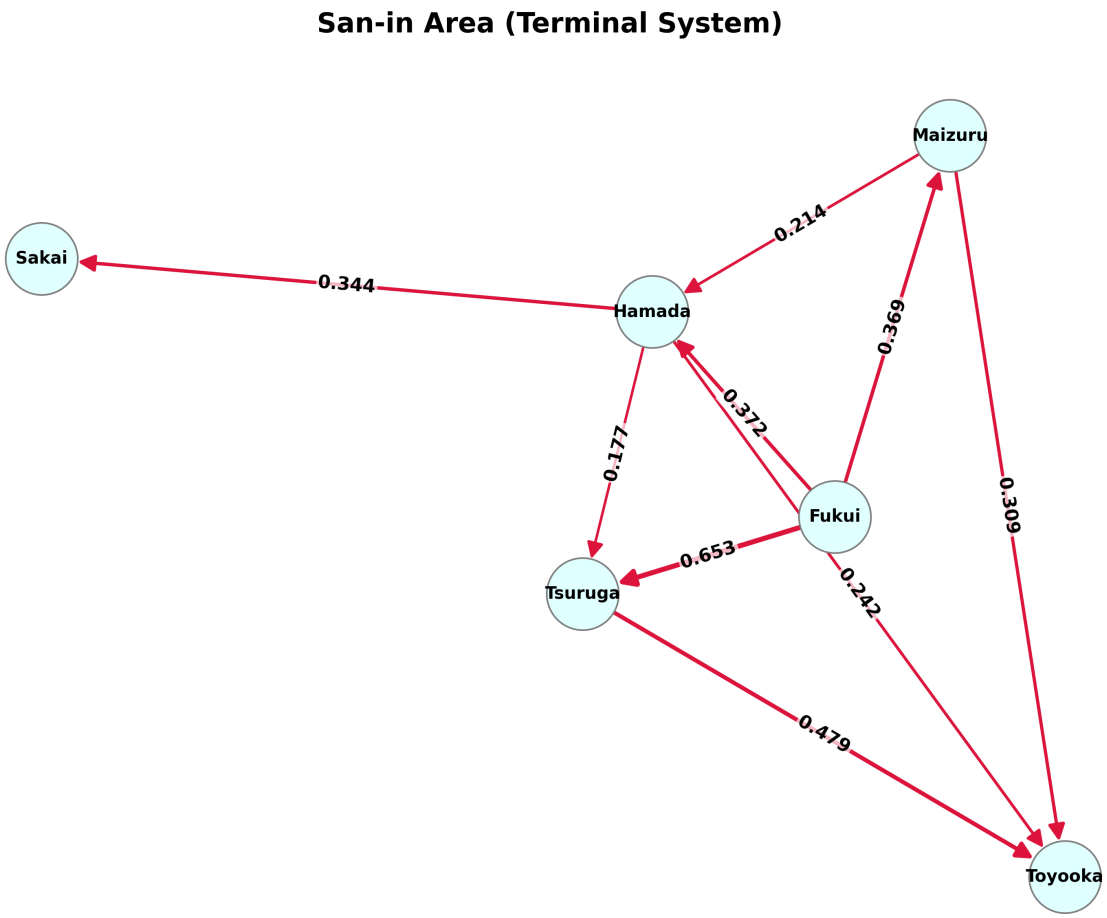

Figure 9: Directed Acyclic Graph (DAG) of the extreme snowfall extracted by LiNGAM for the San-in Area (Terminal System), revealing the causal wave propagation processes within this localized sub-network. The thickness of the arrows indicates the magnitude of the connection coefficients. Red solid arrows denote positive connection coefficients, implying strong positive synchronization and simultaneous amplification under the same weather system.

4.3 Decadal Regime Shifts and Hidden Climate States

To overcome the fundamental limitations of conventional linear trend analysis and eliminate the influence of extreme anomalies, we applied robust regression and state-space modeling (Kalman filtering). Figure 10 compares the long-term trends estimated by ordinary least squares (OLS) and robust regression for Kanazawa and Sapporo. As clearly shown, robust regression effectively mitigates the excessive influence of extreme outliers (e.g., the unprecedented heavy snowfalls in 1963 and 1981), successfully extracting a more stable and reliable baseline.

Building upon this, Figures 11 and 12 demonstrate the non-linear, hidden climate states extracted by the state-space model across the 23 stations. Unlike the simple monotonic decrease suggested by OLS, the smoothed trends vividly capture decadal-scale climate natural variabilities. A striking feature in the core heavy snowfall regions (e.g., Kanazawa, Nagaoka, and Takada) is the dome-shaped peak of extreme snowfall spanning from the 1960s to the mid-1980s, followed by an abrupt, discontinuous decline (regime shift) in the late 1980s.

From a climatological perspective, this abrupt decline in the extracted hidden states perfectly coincides with a well-documented hemispheric-scale climate regime shift that occurred in the late 1980s [13, 14]. During this period, the East Asian Winter Monsoon Index (MOI) reversed from a positive to a negative phase, indicating a weakening of the winter monsoon, while the Arctic Oscillation Index (AOI) jumped to a positive phase, leading to a reduction in cold air outbreaks over the Japanese archipelago [13, 14, 16].

Our state-space model reveals a geographical asymmetry in this regime shift. While the rapid decline in extreme snow depth is most pronounced in the Hokuriku and Niigata regions, stations in Hokkaido (e.g., Sapporo and Asahikawa) exhibit no such sharp decrease, demonstrating relatively stable fluctuations. This contrast stems from regional differences in winter mean temperatures. In the Hokuriku region, winter temperatures hover marginally below the critical threshold distinguishing snow from rain [14, 16]. Consequently, the slight atmospheric warming associated with the macro-scale regime shift in the late 1980s altered the precipitation phase from snow to rain, triggering a rapid decline in extreme snowfall. In contrast, temperatures in the Hokkaido region remain well below freezing; thus, the precipitation phase is insensitive to marginal warming and continues to fall as snow, resulting in minimal fluctuations in extreme snow depth.

These findings suggest that our state-space modeling approach can not only remove observational noise and interpolate past missing data but also relatively accurately reproduce decadal-scale climate regime shifts and the associated local thermodynamic responses.

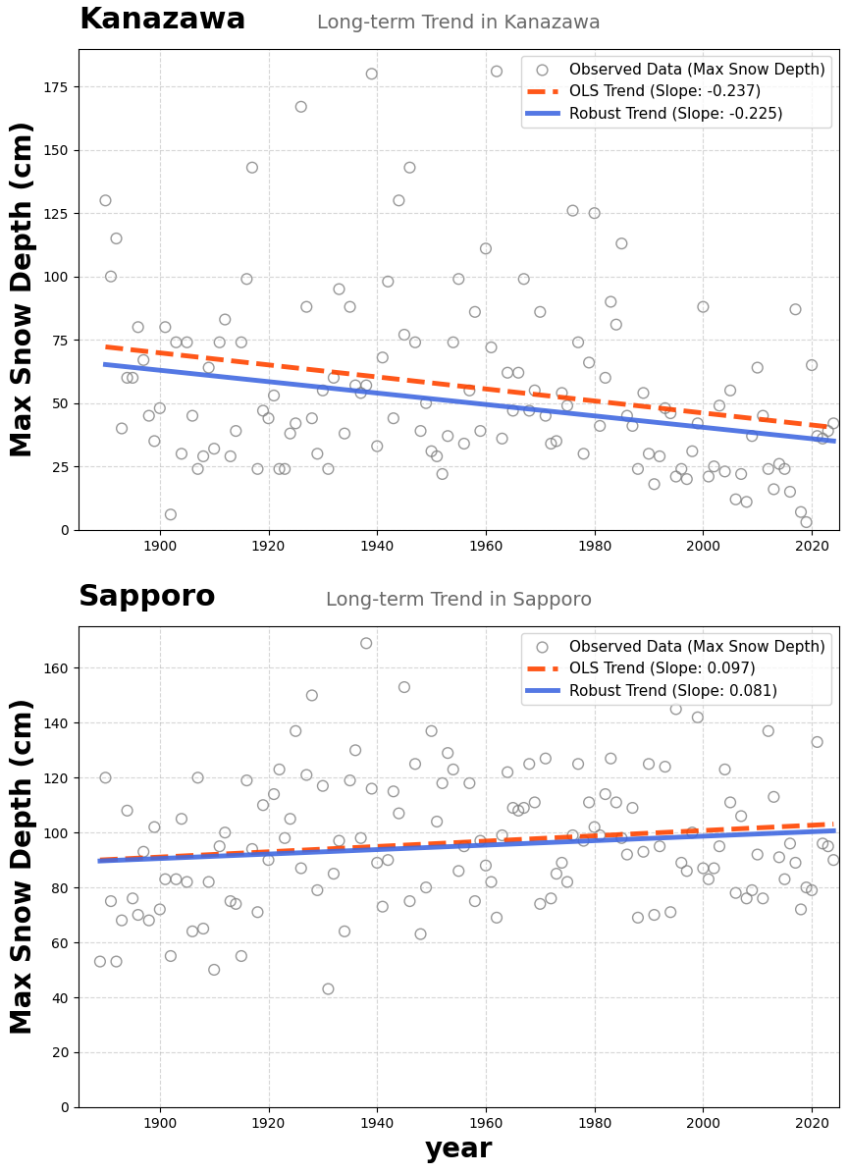

Figure 10: Comparison of long-term trends estimated by OLS and robust regression for Kanazawa and Sapporo. Open circles represent the observed annual maximum snow depth. Red dashed lines show the trends estimated by Ordinary Least Squares (OLS), and blue solid lines show the trends estimated by robust regression, which mitigates the influence of extreme outliers.

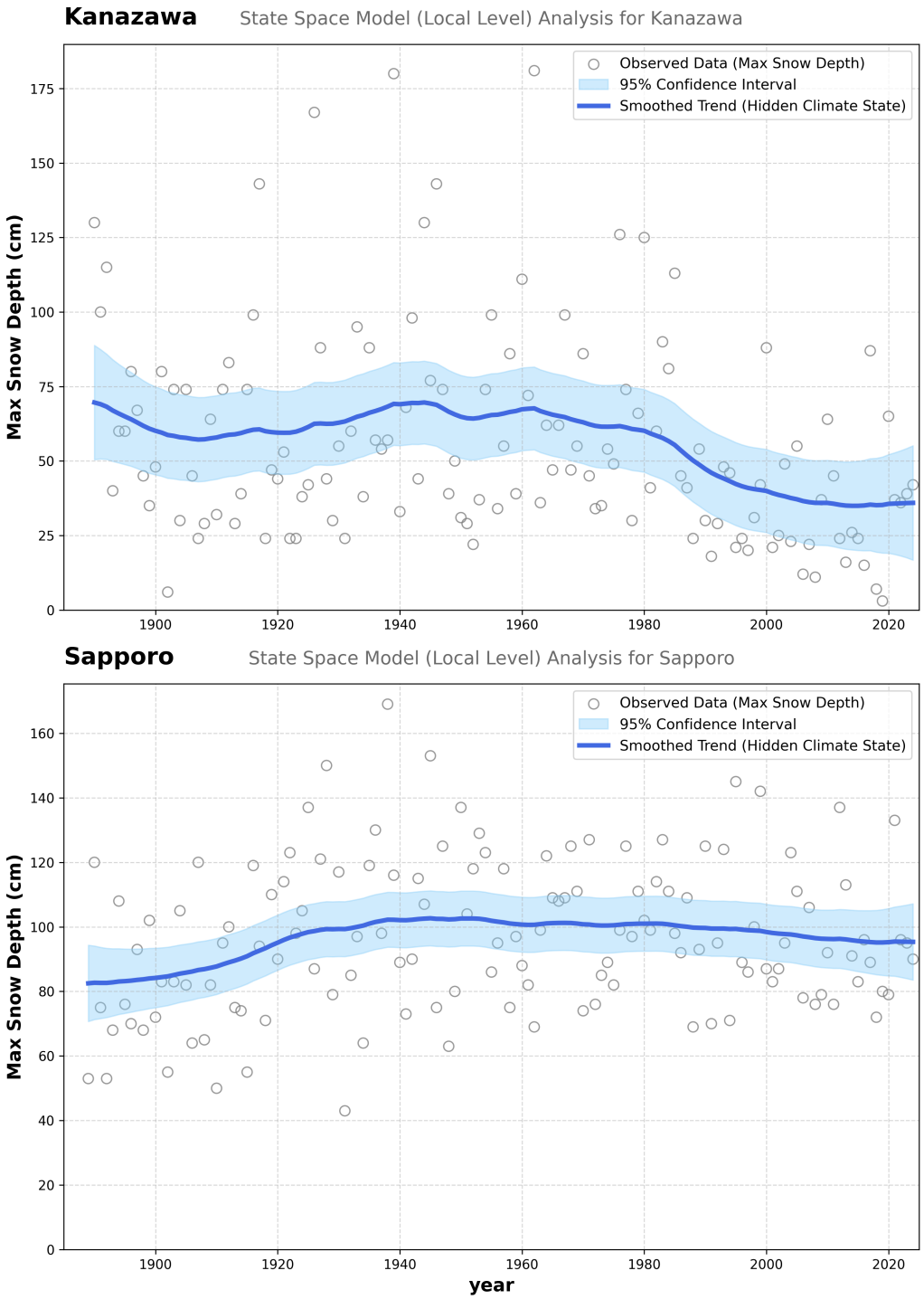

Figure 11: State Space Model (Local Level) Analysis for Kanazawa and Sapporo. Open circles represent the observed data, blue solid lines represent the smoothed trend (latent state), and light blue shaded areas indicate the 95% confidence intervals.

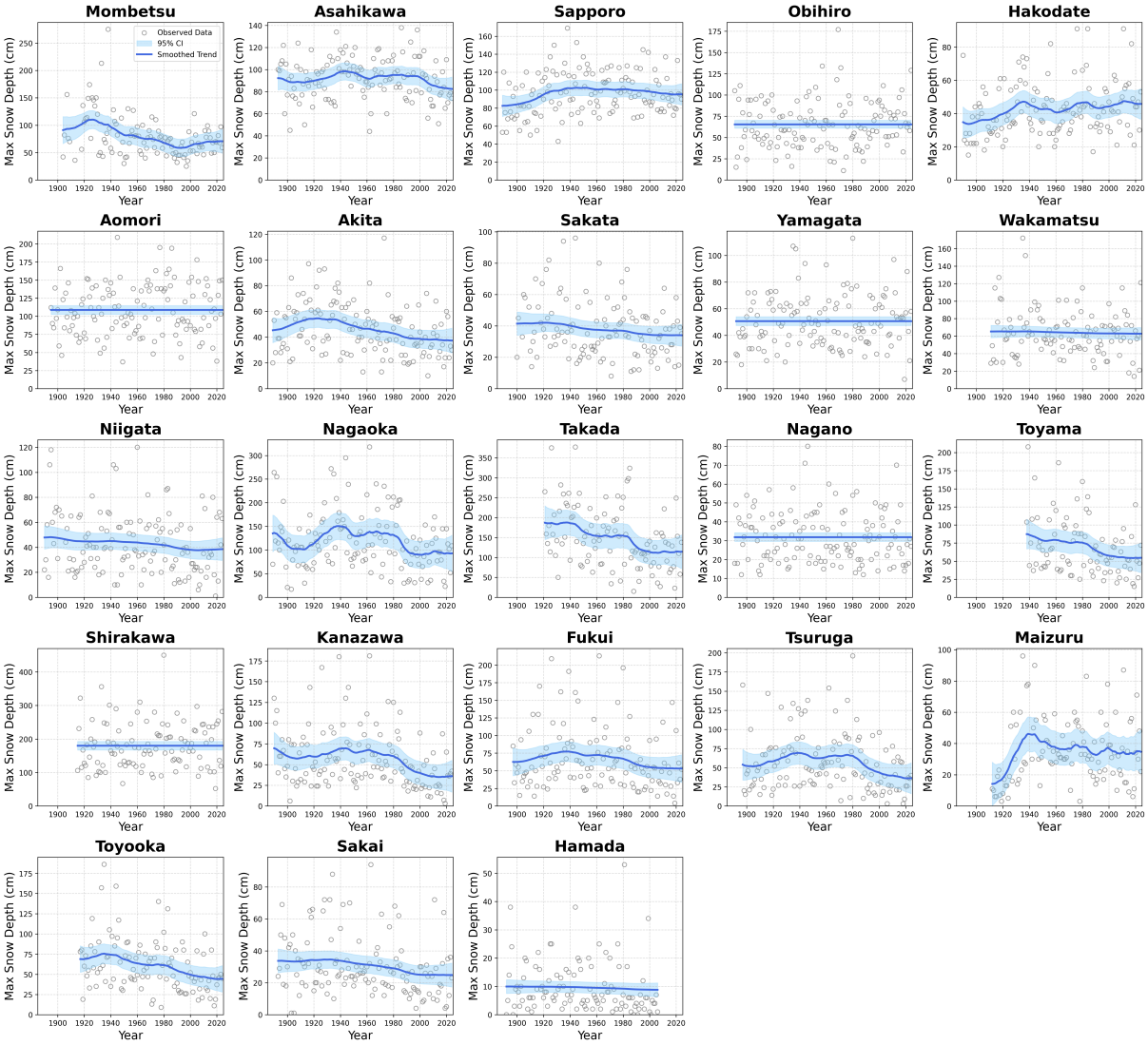

Figure 12: State Space Model (Local Level) Analysis for All 23 Stations. Open circles represent the observed data, blue solid lines represent the smoothed trend, and light blue shaded areas indicate the 95% confidence intervals.

5 Conclusion

In this paper, we proposed a unified data-driven framework for extracting spatiotemporal causal networks and non-linear trends from observational data. Through a representative case study using a 135-year annual maximum snow depth dataset in Japan, we demonstrated robustness to large-scale variability, spurious correlations, extreme outliers, and historical missing values.

The proposed framework explicitly integrates correlation filtering based on Graphical Lasso, non-Gaussian causal discovery via LiNGAM, and non-linear trend extraction using robust state-space modeling. By systematically mitigating large-scale confounding influences, the framework identified local causal propagation processes, including meso-scale inland propagation associated with the Japan-Sea Polar-airmass Convergence Zone (JPCZ) and topographically driven wind shadow effects. Furthermore, the state-space model revealed underlying non-linear climate states and decadal regime shifts that are difficult to capture using conventional linear approaches.

The proposed methodology provides a robust and generalizable foundation for the analysis and modeling of complex spatiotemporal systems, applicable to a wide range of datasets in environmental science and geophysics. While this study extracted decadal-scale non-linear trends, explicitly incorporating global warming effects into extreme value modeling remains an important challenge. Future work will focus on applying non-stationary Generalized Extreme Value (GEV) models to these snow cover network structures, enabling probabilistic evaluation of changes in extreme snowfall under a changing climate.

Table A1: Pearson correlation coefficient matrix for all 23 observation stations.The two-letter abbreviations correspond to the following stations: Mb: Mombetsu, As: Asahikawa, Sp: Sapporo, Ob: Obihiro, Hd: Hakodate, Ao: Aomori, Ak: Akita, Sk: Sakata, Ym: Yamagata, Wk: Wakamatsu, Ni: Niigata, Ng: Nagaoka, Tk: Takada, Nn: Nagano, Ty: Toyama, Sr: Shirakawa, Kz: Kanazawa, Fk: Fukui, Ts: Tsuruga, Mz: Maizuru, To: Toyooka, Sa: Sakai, and Hm: Hamada.

	Mb	As	Sp	Ob	Hd	Ao	Ak	Sk	Ym	Wk	Ni	Ng	Tk	Nn	Ty	Sr	Kz	Fk	Ts	Mz	To	Sa	Hm
Mb	1.000	0.040	0.290	0.210	0.120	0.120	0.190	0.150	0.070	0.030	0.200	0.210	0.260	0.070	0.190	0.060	0.190	0.200	0.120	0.130	0.160	0.070	0.170
As	0.040	1.000	0.220	0.080	0.150	-0.020	0.070	0.060	0.190	0.120	0.160	0.100	0.210	-0.030	0.070	0.030	0.090	0.100	0.190	0.140	0.080	0.030	0.100
Sp	0.290	0.220	1.000	0.200	0.260	0.140	0.240	0.040	0.260	0.130	0.030	0.170	0.200	0.060	0.050	0.150	0.030	0.070	0.110	0.330	0.110	-0.030	0.110
Ob	0.210	0.080	0.200	1.000	0.020	0.040	-0.180	-0.110	0.010	0.060	0.190	-0.090	-0.130	-0.070	-0.110	-0.010	-0.020	-0.060	-0.080	0.040	-0.130	-0.020	0.100
Hd	0.120	0.150	0.260	0.020	1.000	-0.000	0.150	0.270	0.360	0.270	0.170	0.400	0.450	0.090	0.310	0.250	0.190	0.310	0.320	0.360	0.390	0.020	0.120
Ao	0.120	-0.020	0.140	0.040	-0.000	1.000	-0.160	-0.140	-0.030	-0.070	-0.040	-0.050	0.040	-0.020	0.010	0.000	-0.080	-0.110	-0.040	0.060	-0.000	0.290	-0.030
Ak	0.190	0.070	0.240	-0.180	0.150	-0.160	1.000	0.490	0.460	0.380	0.190	0.440	0.520	0.160	0.480	0.380	0.300	0.350	0.370	0.230	0.420	-0.010	0.220
Sk	0.150	0.060	0.040	-0.110	0.270	-0.140	0.490	1.000	0.510	0.460	0.430	0.570	0.550	0.280	0.520	0.440	0.330	0.410	0.420	0.230	0.470	0.040	0.400
Ym	0.070	0.190	0.260	0.010	0.360	-0.030	0.460	0.510	1.000	0.610	0.270	0.490	0.510	0.370	0.570	0.660	0.360	0.450	0.450	0.430	0.490	-0.030	0.220
Wk	0.030	0.120	0.130	0.060	0.270	-0.070	0.380	0.460	0.610	1.000	0.290	0.550	0.450	0.420	0.420	0.560	0.340	0.420	0.450	0.160	0.420	0.000	0.270
Ni	0.200	0.160	0.030	0.190	0.170	-0.040	0.190	0.430	0.270	0.290	1.000	0.500	0.610	0.140	0.640	0.460	0.480	0.510	0.400	0.300	0.320	0.140	0.320
Ng	0.210	0.100	0.170	-0.090	0.400	-0.050	0.440	0.570	0.490	0.550	0.500	1.000	0.790	0.310	0.780	0.680	0.670	0.690	0.670	0.450	0.650	0.100	0.320
Tk	0.260	0.210	0.200	-0.130	0.450	0.040	0.520	0.550	0.510	0.450	0.610	0.790	1.000	0.230	0.750	0.570	0.680	0.690	0.670	0.480	0.640	0.130	0.340
Nn	0.070	-0.030	0.060	-0.070	0.090	-0.020	0.160	0.280	0.370	0.420	0.140	0.310	0.230	1.000	0.220	0.420	0.280	0.300	0.310	0.220	0.380	-0.130	0.180
Ty	0.190	0.070	0.050	-0.110	0.310	0.010	0.480	0.520	0.570	0.420	0.640	0.780	0.750	0.220	1.000	0.700	0.820	0.860	0.730	0.420	0.570	0.080	0.330
Sr	0.060	0.030	0.150	-0.010	0.250	0.000	0.380	0.440	0.660	0.560	0.460	0.680	0.570	0.420	0.700	1.000	0.570	0.680	0.590	0.400	0.470	-0.050	0.280
Kz	0.190	0.090	0.030	-0.020	0.190	-0.080	0.300	0.330	0.360	0.340	0.480	0.670	0.680	0.280	0.820	0.570	1.000	0.890	0.710	0.340	0.550	0.100	0.370
Fk	0.200	0.100	0.070	-0.060	0.310	-0.110	0.350	0.410	0.450	0.420	0.510	0.690	0.690	0.300	0.860	0.680	0.890	1.000	0.780	0.320	0.580	0.030	0.360
Ts	0.120	0.190	0.110	-0.080	0.320	-0.040	0.370	0.420	0.450	0.450	0.400	0.670	0.670	0.310	0.730	0.590	0.710	0.780	1.000	0.440	0.740	0.040	0.320
Mz	0.130	0.140	0.330	0.040	0.360	0.060	0.230	0.230	0.430	0.160	0.300	0.450	0.480	0.220	0.420	0.400	0.340	0.320	0.440	1.000	0.690	-0.070	0.260
To	0.160	0.080	0.110	-0.130	0.390	-0.000	0.420	0.470	0.490	0.420	0.320	0.650	0.640	0.380	0.570	0.470	0.550	0.580	0.740	0.690	1.000	0.010	0.400
Sa	0.070	0.030	-0.030	-0.020	0.020	0.290	-0.010	0.040	-0.030	0.000	0.140	0.100	0.130	-0.130	0.080	-0.050	0.100	0.030	0.040	-0.070	0.010	1.000	0.150
Hm	0.170	0.100	0.110	0.100	0.120	-0.030	0.220	0.400	0.220	0.270	0.320	0.320	0.340	0.180	0.330	0.280	0.370	0.360	0.320	0.260	0.400	0.150	1.000

Table A2: Partial correlation coefficient matrix for all 23 observation stations.

	Mb	As	Sp	Ob	Hd	Ao	Ak	Sk	Ym	Wk	Ni	Ng	Tk	Nn	Ty	Sr	Kz	Fk	Ts	Mz	To	Sa	Hm
Mb	1.000	0.000	0.000	0.000	0.000	0.000	0.000	0.000	0.000	0.000	0.000	0.000	0.000	0.000	0.000	0.000	0.000	0.000	0.000	0.000	0.000	0.000	0.000
As	0.000	1.000	0.000	0.000	0.000	0.000	0.000	0.000	0.000	0.000	0.000	0.000	0.000	0.000	0.000	0.000	0.000	0.000	0.000	0.000	0.000	0.000	0.000
Sp	0.000	0.000	1.000	0.000	0.000	0.000	0.000	0.000	0.000	0.000	0.000	0.000	0.000	0.000	0.000	0.000	0.000	0.000	0.000	0.000	0.000	0.000	0.000
Ob	0.000	0.000	0.000	1.000	0.000	0.000	-0.030	0.000	0.000	0.000	0.000	-0.010	-0.060	0.000	-0.030	0.000	0.000	0.000	0.000	0.000	-0.060	0.000	0.000
Hd	0.000	0.000	0.000	0.000	1.000	0.000	0.000	0.000	0.000	0.000	0.000	0.000	0.000	0.000	0.000	0.000	0.000	0.000	0.000	0.000	0.000	0.000	0.000
Ao	0.000	0.000	0.000	0.000	0.000	1.000	0.000	-0.050	0.000	0.000	0.000	0.000	0.000	0.000	0.000	0.000	0.000	-0.050	0.000	0.000	0.000	0.000	0.000
Ak	0.000	0.000	0.000	-0.030	0.000	0.000	1.000	0.160	0.080	0.000	0.000	0.040	0.070	0.000	0.050	0.000	0.000	0.000	0.000	0.000	0.010	0.000	0.000
Sk	0.000	0.000	0.000	0.000	0.000	-0.050	0.160	1.000	0.060	0.080	0.000	0.120	0.070	0.000	0.080	0.010	0.000	0.000	0.000	0.000	0.040	0.000	0.000
Ym	0.000	0.000	0.000	0.000	0.000	0.000	0.080	0.060	1.000	0.170	0.000	0.020	0.000	0.000	0.020	0.210	0.000	0.000	0.000	0.000	0.050	0.000	0.000
Wk	0.000	0.000	0.000	0.000	0.000	0.000	0.000	0.080	0.170	1.000	0.000	0.060	0.000	0.040	0.000	0.150	0.000	0.000	0.000	0.000	0.000	0.000	0.000
Ni	0.000	0.000	0.000	0.000	0.000	0.000	0.000	0.000	0.000	0.000	1.000	0.000	0.010	0.000	0.160	0.000	0.040	0.050	0.000	0.000	0.000	0.000	0.000
Ng	0.000	0.000	0.000	-0.010	0.000	0.000	0.040	0.120	0.020	0.060	0.000	1.000	0.190	0.000	0.140	0.130	0.070	0.100	0.100	0.000	0.120	0.000	0.000
Tk	0.000	0.000	0.000	-0.060	0.000	0.000	0.070	0.070	0.000	0.000	0.010	0.190	1.000	0.000	0.170	0.000	0.060	0.090	0.080	0.000	0.100	0.000	0.000
Nn	0.000	0.000	0.000	0.000	0.000	0.000	0.000	0.000	0.000	0.040	0.000	0.000	0.000	1.000	0.000	0.090	0.000	0.000	0.000	0.000	0.000	0.000	0.000
Ty	0.000	0.000	0.000	-0.030	0.000	0.000	0.050	0.080	0.020	0.000	0.160	0.140	0.170	0.000	1.000	0.160	0.200	0.190	0.110	0.000	0.040	0.000	0.000
Sr	0.000	0.000	0.000	0.000	0.000	0.000	0.000	0.010	0.210	0.150	0.000	0.130	0.000	0.090	0.160	1.000	0.020	0.130	0.070	0.000	0.010	0.000	0.000
Kz	0.000	0.000	0.000	0.000	0.000	0.000	0.000	0.000	0.000	0.000	0.040	0.070	0.060	0.000	0.200	0.020	1.000	0.300	0.150	0.000	0.000	0.000	0.000
Fk	0.000	0.000	0.000	0.000	0.000	-0.050	0.000	0.000	0.000	0.000	0.050	0.100	0.090	0.000	0.190	0.130	0.300	1.000	0.180	0.000	0.040	0.000	0.000
Ts	0.000	0.000	0.000	0.000	0.000	0.000	0.000	0.000	0.000	0.000	0.000	0.100	0.080	0.000	0.110	0.070	0.150	0.180	1.000	0.000	0.230	0.000	0.000
Mz	0.000	0.000	0.000	0.000	0.000	0.000	0.000	0.000	0.000	0.000	0.000	0.000	0.000	0.000	0.000	0.000	0.000	0.000	0.000	1.000	0.230	0.000	0.000
To	0.000	0.000	0.000	-0.060	0.000	0.000	0.010	0.040	0.050	0.000	0.000	0.120	0.100	0.000	0.040	0.010	0.000	0.040	0.230	0.230	1.000	0.000	0.000
Sa	0.000	0.000	0.000	0.000	0.000	0.000	0.000	0.000	0.000	0.000	0.140	0.100	0.130	-0.130	0.080	-0.050	0.100	0.030	0.040	-0.070	0.010	1.000	0.150
Hm	0.000	0.000	0.000	0.000	0.000	0.000	0.000	0.000	0.000	0.000	0.320	0.320	0.340	0.180	0.330	0.280	0.370	0.360	0.320	0.260	0.400	0.150	1.000

A Markov blankets extracted individually for all 23 observation stations

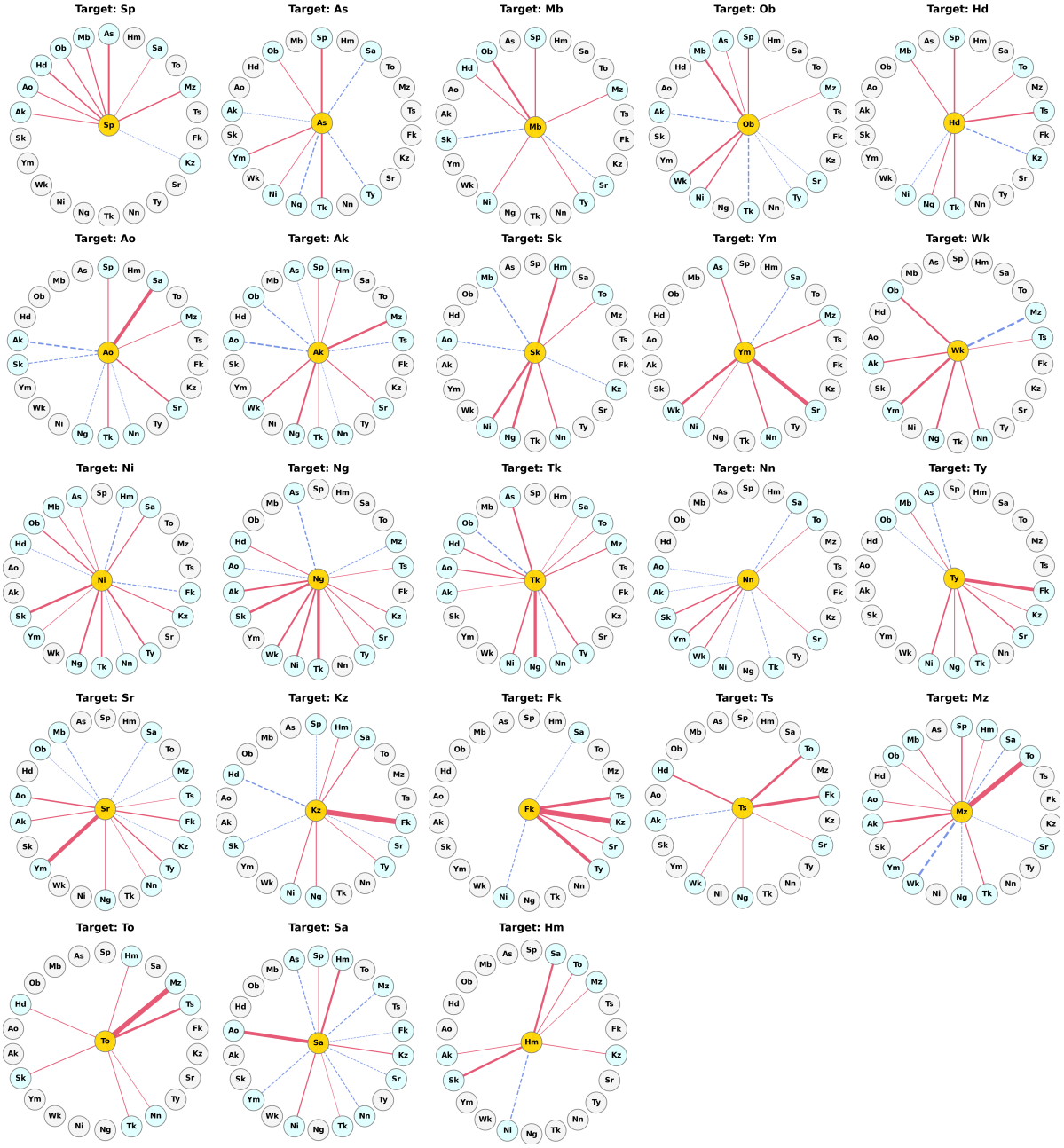

Figure A1: Markov blankets extracted individually for all 23 observation stations, providing a comprehensive overview of the localized subnetworks.Red solid lines indicate positive partial correlations, while blue dashed lines indicate negative partial correlations. The two-letter abbreviations correspond to the following stations: Mb: Mombetsu, As: Asahikawa, Sp: Sapporo, Ob: Obihiro, Hd: Hakodate, Ao: Aomori, Ak: Akita, Sk: Sakata, Ym: Yamagata, Wk: Wakamatsu, Ni: Niigata, Ng: Nagaoka, Tk: Takada, Nn: Nagano, Ty: Toyama, Sr: Shirakawa, Kz: Kanazawa, Fk: Fukui, Ts: Tsuruga, Mz: Maizuru, To: Toyooka, Sa: Sakai, and Hm: Hamada.

References

[1] Avanzi, F., Zheng, Z., Coogan, A., Rice, R., Akella, R., and Conklin, M. H. (2020). Gap-filling snow-depth time-series with Kalman Filtering-Smoothing and Expectation Maximization: Proof of concept using spatially dense wireless-sensor-network data. *Cold Regions Science and Technology*.

[2] Friedman, J., Hastie, T., and Tibshirani, R. (2008). Sparse inverse covariance estimation with the graphical lasso. *Biostatistics*, 9(3), 432-441.

[3] Fujisawa, H. (2017). *Robust Statistics: How to Deal with Outliers*. Kindai Kagaku Sha, Tokyo, 178pp. (in Japanese)

[4] Kalman, R. E. (1960). A new approach to linear filtering and prediction problems. *Journal of Basic Engineering*, 82(1), 35-45.

[5] Kameda, T., Kuwasako, T., and Shirakawa, T. (2023). Characteristics of snow depth and period variations in snowy areas in Japan for 60 years from 1962 to 2021 winter season using annual average snow depth and annual maximum snow depth. *Seppyo*, 85(4), 199-222. (in Japanese)

[6] Kawase, H. (2019). Impacts of global warming on snowfalls and snow covers in Japan. *Seppyo*, 81, 193-205. (in Japanese)

[7] Liu, X.-Q., and Liu, X.-S. (2018). Markov blanket and Markov boundary of multiple variables. *Journal of Machine Learning Research*, 19, 1-50.

[8] Nomura, S. (2016). *Kalman Filter: Time Series Prediction and State Space Model Using R*. Kyoritsu Shuppan, Tokyo, 163pp. (in Japanese)

[9] Shimizu, S., Hoyer, P. O., Hyvärinen, A., and Kerminen, A. (2006). A linear non-Gaussian acyclic model for causal discovery. *Journal of Machine Learning Research*, 7, 2003-2030.

[10] Shimizu, S., Inazumi, T., Sogawa, Y., Hyvärinen, A., Kawahara, Y., Washio, T., Hoyer, P. O., and Bollen, K. (2011). DirectLiNGAM: A direct method for learning a linear non-Gaussian acyclic model. *Journal of Machine Learning Research*, 12, 1225-1248.

[11] Slater, A. G., and Clark, M. P. (2006). Snow data assimilation via an ensemble Kalman filter. *Journal of Hydrometeorology*, 7, 478-493.

[12] Suzuki, H. (2006). Long-term changes of snowfall and snow cover in and around Niigata Prefecture from 1927 to 2005. *Tenki*, 53, 185-196. (in Japanese)

[13] Suzuki, H. (2012). Long-term changes of heavy snowfall in Japan and its relation with environmental fields - Analysis using daily snow depth data of JMA and railways. *Tenki*, 59, 333-350. (in Japanese)

[14] Suzuki, H. (2023). Long-term variations of snowfall and snow cover in Japan and their relationships with environmental fields. *Seppyo*, 85(5), 293-311. (in Japanese)

[15] Tachibana, Y., Honda, M., Nishikawa, H., Kawase, H., Yamanaka, H., Hata, D., and Kashino, Y. (2022). High moisture confluence in Japan Sea polar air mass convergence zone captured by hourly radiosonde launches from a ship. *Scientific Reports*, 12(1), 21674.

[16] Takahashi, H. G. (2021). Long-term trends in snowfall characteristics and extremes in Japan from 1961 to 2012. *International Journal of Climatology*, 41, 2316-2329.

[17] Yamazaki, A., Honda, M., and Kawase, H. (2019). Regional snowfall distributions in a Japan-Sea side area of Japan associated with jet variability and blocking. *Journal of the Meteorological Society of Japan*, 97(1), 205-226.

[18] Yoshizaki, M., and Kato, T. (2007). *Meteorology of Heavy Rain and Heavy Snow*. Asakura Publishing, Tokyo, 187pp. (in Japanese)